Merging of two plumes from area sources with applications to cooling towers

Shuo Li* and M. R. Flynn
Department of Mechanical Engineering, University of Alberta, Edmonton, Alberta, Canada T6G 1H9

(Received 28 January 2020; accepted 21 April 2020; published 15 May 2020)

Velocity potential contours have been used to demarcate the boundary between the interior and exterior of a plume, this for the case of adjacent plumes subject to merger [Rooney, J. Fluid Mech. **771**, R1 (2015)]. Whereas Rooney's theory is restricted to cases where the plume source is much smaller than the distance between neighboring plume centers, the modification suggested herein allows individual plumes to originate from an area source of arbitrary size. In the present theory, the height at which two plumes fully merge is defined as the location where the combined plume boundary is no longer concave. Referencing the plume boundary curvature, we introduce an alternative, simpler entrainment formulation that does not involve the flux-balance parameter used in Rooney's revised model. The present model is applied to adjacent cooling tower plumes and generates satisfactory agreement with previous model predictions, including those that adopt a quite different criterion for plume merger.

DOI: 10.1103/PhysRevFluids.5.054502

I. INTRODUCTION

The merging of jets or plumes is observed in many situations, such as multiport diffusers [1], natural ventilation [2], and cooling tower plumes [3]. In the case of natural ventilation, Linden and Kaye [4] argued that the merging of coflowing plumes can be important in tall, naturally ventilated rooms of high occupancy. For industrial cooling towers commonly arranged in inline or back-to-back configurations [5], plume merger influences the amount of entrainment and, by extension, the dilution rate and the visible plume length. In turn, a correct estimation of the visible plume length is crucial in evaluating possible risks to nearby infrastructure, e.g., due to ice accretion as well as strategies for plume abatement.

The process of plume merger is illustrated in Fig. 1. A number of theoretical models on plume merger, starting with Taylor [6], are based on the idea that the external flow field can be approximated as irrotational. Because irrotational flow is governed by Laplace's equation, which is linear, it is straightforward to superpose two different sinks corresponding to two different entraining plumes. Kaye and Linden [7] investigated the merging of two axisymmetric plumes of equal and unequal strengths using a combination of theory and experiment. Their model assumes that each plume is passively advected by the entrainment flow field of the opposite plume, ambient entrainment being the mechanism responsible for drawing the plumes together. Meanwhile, the merging height in their laboratory experiments is defined as the height where there first appears a single maximum in the transverse buoyancy profile. Following the work of Kaye and Linden [7], Cenedese and Linden [8] proposed a model that parameterizes the mutual entrainment of side by side plumes over a vertical range spanning first contact to full plume merger. Over this range of heights, they found that the plume volume flux varies linearly with height. Their novel contribution was to use a single equation (i.e., their 2.12) to represent the evolution of volume flux of two merging

*shuo10@ualberta.ca

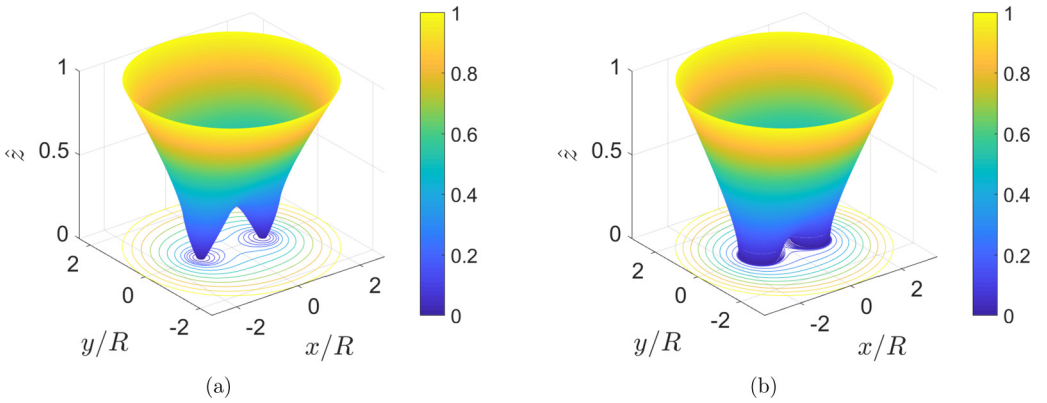

FIG. 1. Surface plots illustrating plume merger from small [(a) $\rho_0 = 0.1$] and large [(b) $\rho_0 = 0.6$] sources with $\Gamma_0 = 1$. The parameters, ρ_0, Γ_0, x/R, y/R, and $\hat{z}$, are defined in Sec. II. Note that these results are produced using a so-called curvature method, which is outlined in Sec. III.

plumes. Unlike the small initial momentum and buoyancy fluxes studied by Kaye and Linden [7] and Cenedese and Linden [8], which, in turn, suggest source conditions close to those of an ideal plume, Lai and Lee [9] investigated the merging of buoyant jets with an excess of momentum compared to pure plumes. Before merger, the individual jet elements are represented by a distribution of point sinks and the dynamic pressure field can be described using Bernoulli's equation. This pressure calculation is used in conjunction with the integral governing equations to derive an updated jet trajectory. A revised pressure field is then computed and the process is repeated until the solution converges—see their Fig. 4. After merger, the velocity and scalar concentration fields are resolved by superposition of momentum or kinetic energy and scalar mass flux, respectively. The validity of Lai and Lee's model was verified by comparison with the output from a RANS-based numerical model employing a k-ϵ turbulence closure [10]. A similar superposition method was adapted by Yannopoulos [11] to predict the mean vertical velocity and concentration of a finite number of interacting buoyant jets.

More recently, Rooney [12] (hereafter R15) proposed using the contours of velocity potential to represent the mean flow boundaries for a long row of plumes or jets. Previous models (e.g., Ref. [11]) assume that the plumes are deflected but that their cross sections remain circular and overlap when merging occurs. By contrast, R15 allows the plume cross section to distort as a result of reduced entrainment. His model prediction generates good agreement with the experimental results of Bush and Woods [13] regarding the depth of the two-dimensional outflow resulting from plume rise in a restricted channel. Later Rooney [14] (hereafter, R16) applied the same approach to study the merging of a number of plumes equally spaced along the perimeter of a circle. The other novel contribution in R16 compared to R15 is the introduction of a modified entrainment assumption, which considers the effect of a so-called flux-balance parameter, Γ (defined and discussed in Sec. II C 2). The R16 model, referred to below as Rooney's revised model to distinguish it from the original model presented in R15, matches satisfactorily with the experimental measurements of the total volume flux of two merging plumes made by Cenedese and Linden [8]. R16 has been recently employed by He and Lou [15] to study the interaction of multiple forced plumes in a linearly stratified ambient. One possible limitation of Rooney's work is that the plume source is assumed to be small compared to the separation distance between neighboring plume centers. In many cases of practical interest (e.g., cooling towers), however, the plume source diameter is nontrivial and the plumes are relatively closely spaced. Under such conditions, a virtual origin correction cannot be applied because the cross section of an individual plume arising from

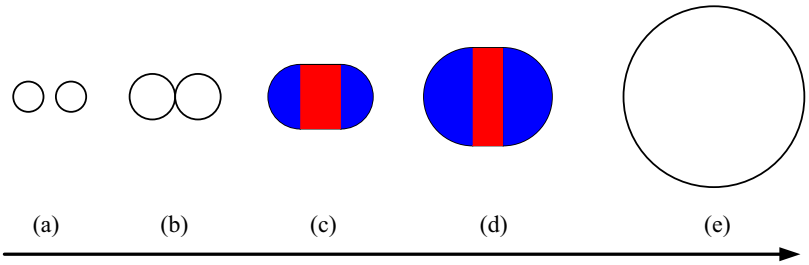

FIG. 2. Evolution of the plume cross section as described by Wu and Koh [3]. Panel (a) denotes the initial stage of two individual plumes. Panel (b) denotes the stage of first contact, however, no plume interaction occurs until full merger, which is depicted in panel (c) and which is defined as the elevation where the area of the central rectangle (shaded red) equals the sum of the areas of the two half round plumes (shaded blue). Panel (d) denotes a stage of the combined plume post merger. Panel (e) shows an axisymmetric plume in the very far field.

the virtual source is expected to be highly distorted by the time it reaches the level of the actual (circular) source.

In the context of cooling tower plumes, a number of merging criteria have been proposed. Davis [16] assumed that the plumes originating from middle cells are affected only slightly by the total number of cells, i.e., end effects can be ignored. In coming to this conclusion, Davis [16] assumed *a priori* a smooth temperature profile along the axis of the merging plumes (see his Fig. 7). As illustrated schematically in Fig. 2, Wu and Koh [3] (hereafter, WK78) proposed a merging criterion on the basis of purely geometrical considerations; their criterion has been employed in various follow-up studies (e.g., Refs. [17,18]). Unfortunately, the interaction between plumes and the associated reduced entrainment due to plume merger are not accounted for, which possibly underestimates the visible plume length.

In the current study, we extend the potential flow theory of R15 and R16 to model the merging of two plumes rising from arbitrary area sources. An alternate entrainment assumption, which considers only the evolution of the plume boundary, is proposed. On this basis, we apply our theory to the merging of two industrial cooling tower plumes. Comparisons with the complementary theory of WK78 are then drawn.

Our manuscript is organized as follows: In Sec. II, we review Rooney's potential flow theories. A novel entrainment formulation that relates the entrainment coefficient to the plume boundary curvature is proposed in Sec. III. In Sec. IV, we modify Rooney's analysis to include finite source effects. Thereafter, in Sec. V we adapt the present model to cooling tower plumes. Finally, in Sec. VI we draw conclusions.

II. ROONEY'S THEORY

A. Complex potential

Following R16, the complex potential due to two equal line sinks (Fig. 3 with $\rho_0 \to 0$) reads

$$\Omega = -\frac{m}{2\pi}\ln(Z'^2 - 1) - \frac{m}{2\pi}\ln R^2 + \Pi, \tag{1}$$

where $-m(Z)$ is the strength of each line sink with $Z = x + \mathrm{i}y = r\,\mathrm{e}^{\mathrm{i}\theta}$, $Z' = x/R + \mathrm{i}y/R = \rho\,\mathrm{e}^{\mathrm{i}\theta}$. Here R is half of the distance between the line sink sources and Π is an arbitrary constant. Due to the symmetry of the flow field, only the sector for which $-\pi/2 \leqslant \theta \leqslant \pi/2$ is considered. The contours of velocity potential are given by $|Z'^2 - 1| = k$, where $k > 0$ is a constant. Stated in terms of radius and polar angle, the velocity potential contours satisfy

$$\rho^4 - 2\rho^2\cos 2\theta + 1 = (\rho^2 + 2\rho\cos\theta + 1)(\rho^2 - 2\rho\cos\theta + 1) = k^2. \tag{2}$$

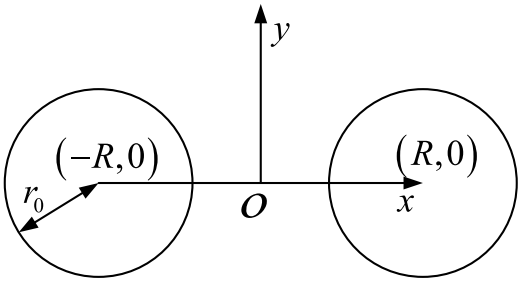

FIG. 3. Sketch of two plumes from an area source of radius r_0. As $r_0 \to 0$, the flow becomes identical to the $n = 2$ case exhibited in Fig. 1 of R16.

Solving for ρ and θ yields

$$\rho = [\cos 2\theta \pm (k^2 - \sin^2 2\theta)^{1/2}]^{1/2}, \tag{3}$$

$$\theta = \pm\frac{1}{2}\cos^{-1}\left(\frac{\rho^4 + 1 - k^2}{2\rho^2}\right), \tag{4}$$

where the negative square root in Eq. (3) is to be considered only when $k \leqslant 1$. Meanwhile, $k^2 - \sin^2 2\theta \geqslant 0$ ($k \leqslant 1$) specifies the limit of polar angle to be determined in Eq. (9). Sample contours of velocity potential are illustrated in Fig. 4.

Differentiating Eq. (2) with respect to θ yields

$$\frac{d\rho}{d\theta} = \frac{\rho \sin 2\theta}{\cos 2\theta - \rho^2}, \tag{5}$$

thus $\rho_{\max}$ occurs at $\theta = 0$, which corresponds to the positive square root in Eq. (3), i.e.,

$$\rho_{\max} = (k + 1)^{1/2}. \tag{6}$$

Analogous to $\rho_{\max}$, it is helpful to consider the minimum radial length, $\rho_{\min}$. When $k < 1$, $\rho_{\min}$ is determined by setting $\theta = 0$ and considering the negative square root in Eq. (3). When $k = 1$,

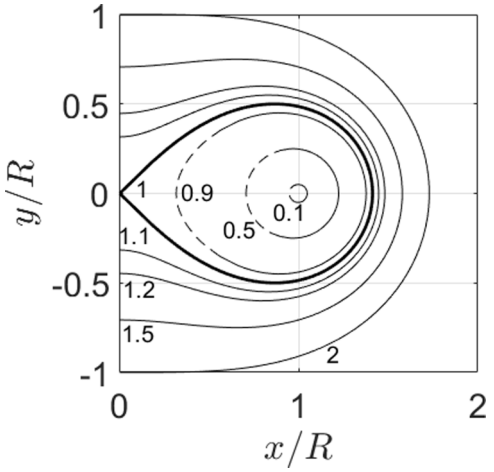

FIG. 4. Contours of velocity potential in Z' space. The numerical values of k are labeled. For closed contours with $k \leqslant 1$, the dashed (solid) curves represent the negative (positive) square root in Eq. (3).

$\rho_{\min} = 0$. Finally, when $k > 1$, we consider $\theta = \pm\pi/2$ and the positive square root in Eq. (3). Altogether,

$$\rho_{\min} = \begin{cases} (1-k)^{1/2}, & k \leqslant 1, \\ (k-1)^{1/2}. & k > 1. \end{cases} \tag{7}$$

For $k \leqslant 1$, the contours are closed and bounded by a polar angle $|\theta_{\lim}| < \pi/2$. The contour coordinates at $\theta_{\lim}$, $(\rho_{\lim}, \theta_{\lim})$, are determined by setting $\frac{d\theta}{d\rho} = 0$. Thus, it may be shown from Eq. (5) that $\rho_{\lim}^2 = \cos 2\theta_{\lim}$. Applying Eq. (3), we find that

$$\rho_{\lim} = (1-k^2)^{1/4}, \tag{8}$$

$$\pm\theta_{\lim} = \pm\tfrac{1}{2}\sin^{-1} k. \tag{9}$$

The maximum closed contour occurs when $k = 1$ with an angular range $-\pi/4 \leqslant \theta \leqslant \pi/4$. Note also that $k = 1$ represents the point of first contact. Accordingly, we define the height of first contact as the height corresponding to $k = 1$.

B. Flow speed, flux, and area integrals

The complex velocity can be obtained from Eq. (1) as

$$u - iv = \frac{d\Omega}{dZ} = -\frac{m}{2\pi R}\frac{2\rho[(\rho^2\cos\theta - \cos\theta) - i(\rho^2\sin\theta + \sin\theta)]}{\rho^4 - 2\rho^2\cos 2\theta + 1}. \tag{10}$$

With this result in hand, the orthogonality between the streamlines and the contours of velocity potential can be confirmed by noting that

$$\frac{dy}{dx} = \frac{(1-\rho^2)\cos\theta}{(1+\rho^2)\sin\theta} = -\frac{u}{v}. \tag{11}$$

The square of the flow speed is given by

$$q^2 = \left|\frac{d\Omega}{dZ}\right|^2 = \frac{m^2}{4\pi^2R^2}\frac{4\rho^2}{\rho^4 - 2\rho^2\cos 2\theta + 1}. \tag{12}$$

Thus, using Eq. (2),

$$q = \frac{m}{2\pi R}\frac{2\rho}{k}. \tag{13}$$

At $\rho = \rho_{\max}$, the flow speed is

$$q_e = \frac{m}{2\pi R}\frac{2(k+1)^{1/2}}{k}, \tag{14}$$

which is the maximum speed of the entrained flow along a velocity potential contour. Finally, the cross-sectional area enclosed by a velocity potential contour is calculated as follows:

$$A' \equiv \frac{A}{R^2} = \begin{cases} 2\int_{\rho_{\min}}^{\rho_{\max}} \theta_+ \rho\, d\rho, & k \leqslant 1, \\ \frac{1}{2}\int_{-\pi/2}^{\pi/2} \rho_+^2\, d\theta, & k > 1, \end{cases} \tag{15}$$

where ρ_+ and θ_+ refer to the different solutions in Eqs. (3) and (4).

C. Plume theory

1. Generalized plume equations

According to R15 and R16, the plume governing equations are given by

$$A\frac{d}{dz}\left(\frac{1}{2}w^2\right) = Ag' - wE, \tag{16}$$

$$\frac{d}{dz}(Aw) = E, \tag{17}$$

$$\frac{d}{dz}(Awg') = -N^2Aw. \tag{18}$$

Though written in terms of the plume cross-sectional area, A, vertical velocity, w, reduced gravity, g', and the buoyancy frequency, $N = (-\frac{g}{\rho_a}\frac{d\rho_a}{dz})^{1/2}$, where ρ_a is the ambient density and g is gravitational acceleration, the above equations could just as well be expressed using the volume flux, $Q = Aw$, the momentum flux, $M = Aw^2$, the buoyancy flux, $F = Awg'$. In contrast to the novel approach of He and Lou [15], we consider, for simplicity, a neutrally stratified ambient so that the governing equation for buoyancy is trivial and can be omitted. The closure condition to Eqs. (16)–(18) is Taylor's entrainment assumption [19], which relates the entrainment velocity to the vertical velocity of the plume, i.e.,

$$q_e = \alpha\, w, \tag{19}$$

where α is an entrainment coefficient[1] and q_e is assumed to be the maximum speed of the entrained flow as specified by Eq. (14). The flux of ambient fluid entrained into the rising plume is given as

$$E = m = \alpha\, w\, R\, f_e, \tag{20}$$

where

$$f_e = \frac{\pi k}{(k+1)^{1/2}}. \tag{21}$$

2. Modified entrainment assumption

To further characterize the plume, we follow Morton [22] and introduce a parameter Γ that describes how forced or lazy a plume is, defined as

$$\Gamma(z) = \frac{5}{8\,\alpha\,\pi^{1/2}}\frac{Q^2\,F}{M^{5/2}}. \tag{22}$$

Γ is equivalent to the local plume Richardson number, and its value indicates the departure of the plume from pure plume balance, a state defined mathematically as $\Gamma(z=0) \equiv \Gamma_0 = 1$ [23]. For $\Gamma_0 \neq 1$, plumes can be classified as forced ($0 < \Gamma_0 < 1$) or lazy ($\Gamma_0 > 1$). In the forced and lazy cases, respectively, there is an excess and deficit of momentum at the source compared to a pure plume. When two plumes merge, according to R16, the flux-balance parameter becomes, $\Gamma_m(z) = 2^{1/2}\Gamma(z)$. Accordingly, Eq. (19) is revised to read

$$q_e = \alpha f_m w, \tag{23}$$

in which

$$f_m = \frac{Sk + 2^{1/2}}{Sk + \Gamma_m}, \tag{24}$$

[1]Note that previously measured values for α presume that the plume is either axisymmetric or two-dimensional. Here, consistent with Fig. 3, we focus on the former geometry and assume a value for α that is z-independent. For a comprehensive discussion on the choice of entrainment coefficient, see Refs. [20,21].

where S is an arbitrary constant with $S = 0.1$ in R16. The two entrainment formulations, Eqs. (19) and (23), correspond to Rooney's original and revised models, respectively.

3. Nondimensionalization

Following R16, Eqs. (16) and (17) can be nondimensionalized using the buoyancy flux F and the distance, $d = 2R$, between plume sources. On this basis, we write

$$w = \alpha^{-1/3} F^{1/3} d^{-1/3} \hat{w}, \quad Q = \alpha^{-1/3} F^{1/3} d^{5/3} \hat{Q}, \quad z = \alpha^{-1} d \hat{z}, \tag{25}$$

where hatted variables carry no units. The flux-balance parameter can be expressed as $\Gamma = \frac{5}{8\pi^{1/2}} \hat{A}^{-1/2} \hat{w}^{-3}$. Thus, the nondimensional form of the governing equations read

$$\frac{d\hat{w}}{d\hat{z}} = \frac{1}{\hat{w}\,\hat{Q}} - \frac{\hat{w}^2}{2\hat{Q}} f_e, \tag{26}$$

$$\frac{d\hat{Q}}{d\hat{z}} = \frac{1}{2}\,\hat{w}\, f_e. \tag{27}$$

The nondimensional cross-sectional area is $\hat{A} = \hat{Q}/\hat{w} = A/d^2 = A'/4$ where A' is defined in Eq. (15). Equations (26) and (27) are solved using a fourth-order Runge-Kutta finite difference method whereby the range of integration is $0.001 \leqslant \hat{z} \leqslant 5$ with a step size of 0.001. Specifically, we first assign an initial guess of small k, e.g., $k = 0.1$, then the (small) source cross-sectional area, A', is obtained from Eq. (15). The source value for $\hat{w}$ is obtained by selecting a value for Γ_0 depending on the nature of the plume under examination (i.e., forced versus pure versus lazy). After each numerical integration step in $\hat{z}$, the value of k can be updated by inverting Eq. (15) using root-finding. It is expected that k increases with z, albeit in a nonlinear fashion. Note that Eqs. (26) and (27) are based on the original model of R15; for the revised model we can simply multiply the term f_e [from Eq. (21)] with f_m [from Eq. (24)] on the right-hand side of both Eqs. (26) and (27).

Because the plume at $\hat{z} = 0.001$ and $k = 0.1$ is not strictly ideal ($\rho_0 \approx 0.05$), a virtual origin correction, i.e., $\hat{z}_{vn}$, is made to better match the numerical solution with the corresponding near-source similarity scaling. For $\Gamma_0 > 0.5$, we follow the formula for $\hat{z}_{vn}$ proposed by Hunt and Kaye [24]. In case of pure plume balance at the source, i.e., $\Gamma_0 = 1$, the location of the virtual origin below the actual source is estimated as $\hat{z}_{vn} \approx 0.02$.

4. Representative results

Considering $\Gamma_0 = 1$, the evolution of vertical velocity ($\hat{w}$) and flux-balance parameter (Γ_m) using both the original and revised models is illustrated in Fig. 5. As shown in Fig. 5(a), the original model predicts a greater vertical velocity than does the revised model with $S = 0.1$. Notably, and for $\hat{z} \gtrsim 0.32$, the vertical velocity using the original model overshoots the far-field similarity solution then approaches it asymptotically. Over this range of heights, Fig. 5(b) reveals that the plume is in a forced plume regime, i.e., $\Gamma_m < 1$, which is a direct consequence of the reduced entrainment associated with the simple entrainment assumption Eq. (19). Conversely, the introduction of f_m tends to increase entrainment when Γ_m is low. For the revised models illustrated in Fig. 5(b), Γ_m with $S = 1$ decreases to a level slightly below unity, whereas Γ_m with $S = 0.1$ remains above unity over the entire range of heights. In general, for the original model and revised model with $S = 1$, the plume follows a relatively nonsmooth "lazy–forced–pure" regime transition. By contrast, for the revised model with $S = 0.1$, the plume follows a more monotone "lazy–pure" regime transition.

III. ALTERNATE FORM FOR f_m

A. Plume-boundary curvature

R15 argued that it should be possible to devise an entrainment assumption that relates the rate of entrainment to the curvature of the plume boundary. This curvature is indicated by the shape

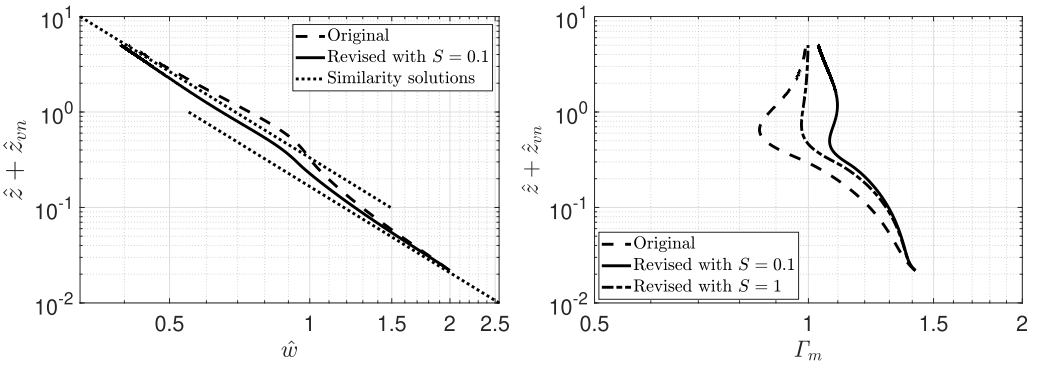

FIG. 5. Evolution of $\hat{w}$ [panel (a)] and Γ_m [panel (b)] as predicted by the original model (dashed curve), revised model with $S = 0.1$ (solid curve) and with $S = 1$ (dash-dotted curve). The dotted lines in (a) denote the near- and far-field self-similarity solutions.

of the velocity potential contours in, e.g., Fig. 4. However, R16 introduced a correction factor, f_m in Eq. (24), with a different goal in mind, i.e., to increase the entrainment when Γ_m decreases and *vice versa*. The revised entrainment assumption proposed by R16 produces good agreement with Cenedese and Linden [8] vis-à-vis the volume flux of two merging plumes. However, it is not altogether obvious whether Γ_m maps straightforwardly to the plume boundary curvature except in the near- and far-field limits where the individual and the merged plumes are axisymmetric. In light of the above, and returning to the suggestion made in R15, we propose that the rate of entrainment, rather than depending on Γ_m, depends instead on the shape of the plume boundary as represented by the shape of the velocity potential contours defined by Eq. (2). Below, we explore this possibility in quantitative detail and thereby derive a new entrainment formulation that is different from the well-established formulations presented in R15 (Rooney's original model) and R16 (Rooney's revised model).

The contour curvature is expressed as

$$\kappa(\theta) = \frac{\left|2\left(\frac{d\rho}{d\theta}\right)^2 + \rho^2 - \rho\frac{d^2\rho}{d\theta^2}\right|}{\left[\left(\frac{d\rho}{d\theta}\right)^2 + \rho^2\right]^{3/2}}. \tag{28}$$

At $\rho = \rho_{\max}$, the curvature simplifies to

$$\kappa_c = \frac{2+k}{k(1+k)^{1/2}}. \tag{29}$$

We measure the departure of the contour from a circular shape using a parameter P, defined as

$$P = \begin{cases} \frac{1}{2}(\rho_{\max} - \rho_{\min})\,\kappa_c, & k \leqslant 1, \\ \rho_{\max}\,\kappa_c, & k > 1. \end{cases} \tag{30}$$

The near- and far-field limits whereby $P \to 1$ as $k \to 0$ and $k \to \infty$ also apply. Even so, there is a discontinuity in P at $k = 1$ because $k = 1$ marks the beginning of the transition from individual plumes to a merged plume. By comparison with Eq. (24), we find in Fig. 6 that the following simple formulation for f_m in terms of P generates equally acceptable behavior:

$$f_m = \begin{cases} P^{n'}, & k \leqslant 1, \\ P^{n''}, & k > 1. \end{cases} \tag{31}$$

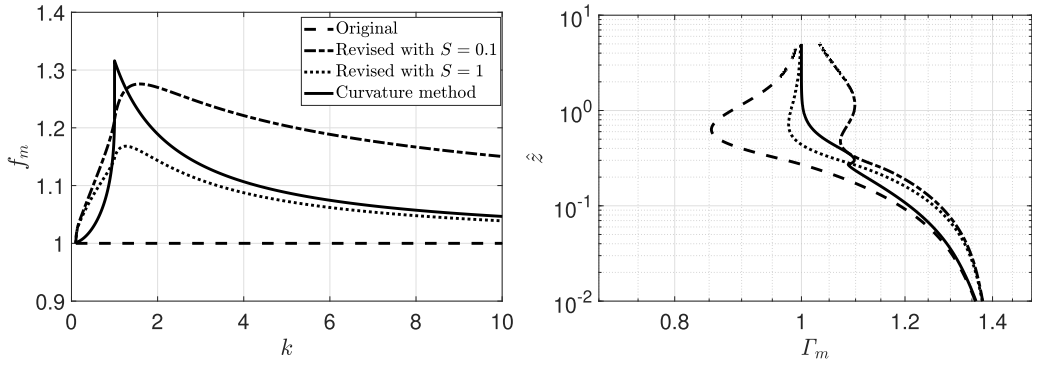

FIG. 6. The evolution of f_m and Γ_m in the original model (dashed line or curve), revised model with $S = 0.1$ (dash-dotted curve) and with $S = 1$ (dotted curve) and the curvature method using Eq. (31) (solid curve). In contrast to Fig. 5(b), a virtual origin correction is not included because the small offset by $\hat{z}_{vn}$ does not significantly alter the positions of the curves.

By an empirical trial-and-error process, and favoring a fractional representation for the exponents n' and n'', we propose that $n' = 1/2$ and $n'' = 1/4$. Note that He and Lou [15] also discussed the plume-boundary curvature but did not propose a functional form like Eq. (31) for f_m. Instead, they proposed a simpler function that reads, for the two plume case,

$$f_m = k^2 \exp(-k^2) + 1. \tag{32}$$

The above formulation also achieves near- and far-field limits of unity; moreover, f_m reaches its maximum value at $k = 1$. Note, however, that for $k > 1$ Eq. (32) converges to unity much more rapidly than do the formulations illustrated in Fig. 6(a). This implies that Eq. (32) may lead to relatively low entrainment post-merger.

Shown in Fig. 6(a) is the correction factor, f_m versus k. For $k \gtrsim 1$, the value of f_m computed using the curvature method lies slightly above that obtained by the revised model with $S = 1$. One advantage of the curvature method is that, as shown in Fig. 6(b), it avoids the oscillation about unity that characterizes both the original model (dashed curve) and the revised model with $S = 1$ (dotted curve). Moreover, Γ_m using the curvature method approaches the far-field similarity solution more rapidly than is the case with the other models considered. This accelerated similarity seems more consistent with the observation of two merging plumes made by Baines [25]. He found that the total volume flux of the two merging plumes rapidly approached the similarity solution once the two plumes began to interact.

B. Height of full merger

As mentioned at the end of Sec. II A, R16 defined the height of first contact, $\hat{z}_{fc}$, which corresponds to $k = 1$. R16 also determined the far-field virtual origin correction, $\hat{z}_{vf}$, which is defined as the height below the actual source where a virtual pure plume with an identical total buoyancy flux can achieve the same far-field similarity solution for the merged plume. What is left unspecified is the height of full merger. Unfortunately, the definition proposed by Kaye and Linden [7], i.e., the height where a single maximum in the transverse buoyancy profile appears, is difficult to apply in the present analysis. For a more straightforward prediction, we shall define the height of full merger on the basis of the velocity potential contours. For $1 \leqslant k < 2$, as illustrated in Fig. 4, the combined plume boundary always exhibits concavity close to $x = 0$. The height of full merger, $\hat{z}_{fm}$, is defined as the height at which the boundary of the combined plume is no longer concave. Stated

TABLE I. Height of full merger predicted by R15, R16, the present analysis and measured/predicted in Kaye and Linden [7].

	Original	Revised with $S = 0.1$ (1)	Curvature	Kaye and Linden [7]	
$\hat{z}_{fm}$	0.61	0.51 (0.54)	0.52	0.49 ± 0.03 ($\alpha = 0.12$)	0.44 (theory)

in mathematical terms, we look for the elevation (or k value) satisfying

$$\kappa(\theta = \pi/2) = \frac{|1 - 2/k|}{(k-1)^{1/2}} = 0, \tag{33}$$

which yields $k = 2$. Therefore, $\hat{z}_{fm}$ is defined as the height corresponding to $k = 2$.

C. Comparison with previous theoretical and experimental results

To test the validity of the definition for the height of full merger, we compare $\hat{z}_{fm}$ predicted by the original and revised models and the curvature method with the theoretical and experimental results of Kaye and Linden [7] in Table I. The nondimensional height of full merger in Kaye and Linden [7] is sensitive to the choice of entrainment coefficient, although $\alpha = 0.09$ was selected therein. We shall instead choose $\alpha \approx 0.12$, as validated by Cenedese and Linden [8]. Meanwhile, Kaye and Linden [7] predicted theoretically that $\hat{z}_{fm} = 0.44$. Table I shows that $\hat{z}_{fm}$ predicted by the revised models and the curvature method match well with this measured result.

R16 compared his original and revised models with the experimental results of Cenedese and Linden [8]. Details of the associated "filling-box" experiment are presented in Sec. 3 of Cenedese and Linden [8] and in Sec. 6 of R16. By reproducing Figs. 6 and 9 of R16 (not shown here) but adding solutions derived from the curvature method, we find, consistent with Fig. 6(a), that the curvature method produces results very close to those derived from the revised model with $S = 1$. From these comparisons with previous theoretical and experimental results, we conclude that the curvature method exhibits comparable performance vis-à-vis Rooney's revised model. It is worth reiterating that the curvature model is simpler than the revised model because the former requires specification only of k, whereas the latter requires specification of both k and Γ_m.

IV. FINITE SOURCE EFFECT

A. Modified contours approximating plume boundaries

We now introduce $\rho_0 = r_0/R > 0$, defined as the ratio of the plume source radius to half of the distance between the plume centers—see Fig. 3. Our analysis proceeds on the basis of the following two assumptions: (i) the complex potential is still given by Eq. (1), and (ii) nonpoint source plumes distort in a manner similar to their point source counterparts. Technical details associated with this latter assumption are briefly summarized in Appendix A. Therefore, and incorporating a finite ρ_0 into Eq. (2), we ultimately arrive at the following analog expression:

$$\rho^4 - 2\rho^2\left(\cos 2\theta + \rho_0^2\right) + \left(\rho_0^2 - 1\right)^2 = \left(\rho^2 + 2\rho\cos\theta + 1 - \rho_0^2\right)\left(\rho^2 - 2\rho\cos\theta + 1 - \rho_0^2\right) = k^2. \tag{34}$$

Solutions to Eq. (34) are presented in Fig. 7 for a pair of ρ_0 values. On the basis of this figure and Eq. (34), we make two important observations. First, Eq. (34) does not admit any contours within the cross section of the plume source. Second, Eq. (34) applies for the case of two adjacent plumes. Results similar to Eq. (34) for cases with $n > 2$ are provided in Appendix B.

Analytical solutions to Eq. (34) are as follows:

$$\rho = \left\{\cos 2\theta + \rho_0^2 \pm \left[k^2 - \sin^2 2\theta + 2\,\rho_0^2(1 + \cos 2\theta)\right]^{1/2}\right\}^{1/2}, \tag{35}$$

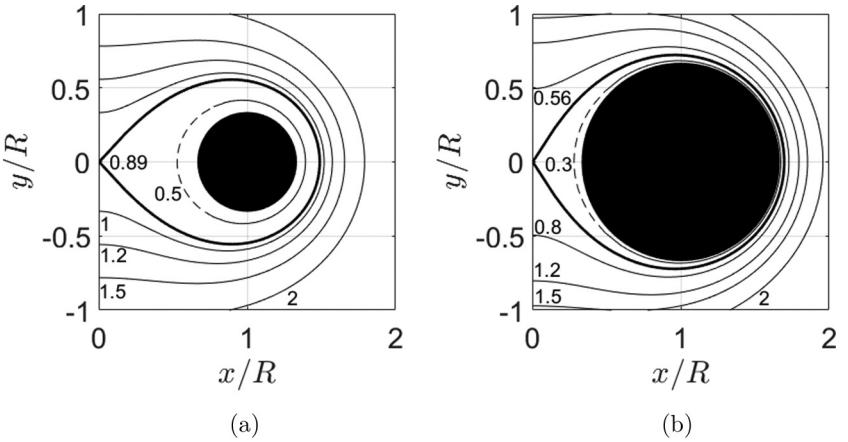

FIG. 7. As in Fig. 4, but with $\rho_0 > 0$. (a) $\rho_0 = 1/3$, (b) $\rho_0 = 2/3$. The closed black circles in both panels denote the plume source.

$$\theta = \pm\frac{1}{2}\cos^{-1}\left[\frac{\rho^4 + \left(\rho_0^2 - 1\right)^2 - k^2}{2\rho^2} - \rho_0^2\right], \tag{36}$$

where the negative square root in Eq. (35) applies for $k < 1 - \rho_0^2$. Analogous to Eq. (3), $k^2 - \sin^2 2\theta + 2\rho_0^2(1 + \cos 2\theta) \geqslant 0$ ($k < 1 - \rho_0^2$) determines the range of polar angles occupied by the closed contours in Fig. 7.

Differentiating Eq. (34) yields

$$\frac{d\rho}{d\theta} = \frac{\rho \sin 2\theta}{\cos 2\theta - \rho^2 + \rho_0^2}, \tag{37}$$

and so the maximum radial extent, now defined as

$$\rho_{\max} = \left(1 + \rho_0^2 + \left(k^2 + 4\rho_0^2\right)^{1/2}\right)^{1/2}, \tag{38}$$

still occurs at $\theta = 0$. However, the minimum radial length is given as

$$\rho_{\min} = \begin{cases} \left(1 + \rho_0^2 - \left(k^2 + 4\rho_0^2\right)^{1/2}\right)^{1/2}, & k \leqslant 1 - \rho_0^2, \\ \left(k - 1 + \rho_0^2\right)^{1/2}, & k > 1 - \rho_0^2. \end{cases} \tag{39}$$

For $k \leqslant 1 - \rho_0^2$, the positions of the limits $(\rho_{\lim}, \theta_{\lim})$ are determined from $d\theta/d\rho = 0$, which gives $\rho_{\lim}^2 = \cos 2\theta_{\lim} + \rho_0^2$. Substituting into Eq. (34) yields, as the respective analogues of Eqs. (8) and (9),

$$\rho_{\lim} = \left[\left(1 - \rho_0^2\right)^2 - k^2\right]^{1/4}, \tag{40}$$

$$\pm\theta_{\lim} = \pm\tfrac{1}{2}\cos^{-1}\left\{-\rho_0^2 + \left[\left(1 - \rho_0^2\right)^2 - k^2\right]^{1/2}\right\}. \tag{41}$$

Note, in particular, that the maximum closed contour when $k = 1 - \rho_0^2$ corresponds to an angular range $-\frac{1}{2}\cos^{-1}(-\rho_0^2) \leqslant \theta \leqslant \frac{1}{2}\cos^{-1}(-\rho_0^2)$.

Analogous to the approach outlined in Sec. III B, the plume curvature at the level of full merger should satisfy

$$\kappa(\theta = \pi/2) = \frac{|1 - 2/k|}{\left(k - 1 + \rho_0^2\right)^{1/2}} = 0, \tag{42}$$

which again yields $k = 2$ as the height of full merger. Meanwhile, and consistent with the $\rho_0 \to 0$ case, $k = 1 - \rho_0^2$ represents the point of first contact.

Under the assumption that the complex potential defined by Eq. (1) applies also to the nonpoint source case, the contours illustrated in Fig. 7 are not, strictly speaking, curves of equi-(velocity) potential. The velocity potential, ϕ, associated with Eq. (1) is expressed for the $\rho_0 > 0$ case as

$$\phi = -\frac{m}{2\pi R} \ln\left(k^2 + 2\rho_0^2\rho^2 - \rho_0^4 + 2\rho_0^2\right)^{1/2}. \tag{43}$$

For small ρ_0, ϕ is approximately constant on each of the contours defined by Eq. (34). For large ρ_0, it can be inferred from Eqs. (38) and (39) that greater variations in ϕ arise, but these are most prominent in the near source region with small k values. In the context of the self-similar model prescribed by Eqs. (16)–(18), this near source region is of less interest than the regions of greater distances from the source. Moreover, and as we explain in greater detail in Sec. IV G below, the contours defined by Eq. (34), which we consider to define the plume boundary when $\rho_0 > 0$, yield good agreement with previous theoretical results of Cenedese and Linden [8] even in the extreme case of $\rho_0 = 1$.

B. Flow speed and cross-sectional area

To be consistent with the $\rho_0 \to 0$ case, and following the justification given in Appendix C, we require that $E = m$ also applies for nonideal line sinks. Accordingly, and with $\rho_0 > 0$, the complex velocity normal to the plume boundary reads

$$\begin{aligned} &u_\perp - iv_\perp \\ &= -\frac{m}{2\pi R} \frac{2\rho\left(k^2 + \rho_0^2\rho^2 - \rho_0^4 + 2\rho_0^2 + \rho_0^2\cos 2\theta\right)\left[\left(\rho^2 - \rho_0^2 - 1\right)\cos\theta - i\left(\rho^2 - \rho_0^2 + 1\right)\sin\theta\right]}{\left(k^2 + 2\,\rho_0^2\,\rho^2 - \rho_0^4 + 2\rho_0^2\right)\left[k^2 + 2\rho_0^2(1 + \cos 2\theta)\right]}. \end{aligned} \tag{44}$$

The flow speed normal to the plume boundary is given by

$$q_\perp = \frac{m}{2\pi R} \frac{2\rho\left(k^2 + \rho_0^2\rho^2 - \rho_0^4 + 2\rho_0^2 + \rho_0^2\cos 2\theta\right)}{\left(k^2 + 2\,\rho_0^2\,\rho^2 - \rho_0^4 + 2\rho_0^2\right)\left[k^2 + 2\rho_0^2(1 + \cos 2\theta)\right]^{1/2}}. \tag{45}$$

Thus, at $\rho = \rho_{\max}$, the speed of the flow entrained across the plume boundary is

$$q_e = \frac{m}{2\pi R} \frac{2\left[1 + \rho_0^2 + \left(k^2 + 4\rho_0^2\right)^{1/2}\right]^{1/2}\left[k^2 + 4\rho_0^2 + \rho_0^2\left(k^2 + 4\rho_0^2\right)^{1/2}\right]}{\left[k^2 + \rho_0^4 + 4\rho_0^2 + 2\rho_0^2\left(k^2 + 4\rho_0^2\right)^{1/2}\right]\left(k^2 + 4\rho_0^2\right)^{1/2}}, \tag{46}$$

which is used to represent the bulk entrainment velocity.

Note finally that plume cross-sectional areas are still defined by Eq. (15). The cross-sectional area as a function of k for different ρ_0 is shown in Fig. 8. In general, A' grows approximately linearly for $k \gtrsim 1$.

C. Entrainment flux

With reference to the original entrainment assumption, i.e., Eq. (19), the entrainment flux with $\rho_0 \geqslant 0$ is given by

$$E = m = \alpha\, w\, R\, f_e, \tag{47}$$

where

$$f_e = \frac{\pi\left[k^2 + \rho_0^4 + 4\rho_0^2 + 2\rho_0^2\left(k^2 + 4\rho_0^2\right)^{1/2}\right]\left(k^2 + 4\rho_0^2\right)^{1/2}}{\left[1 + \rho_0^2 + \left(k^2 + 4\rho_0^2\right)^{1/2}\right]^{1/2}\left[k^2 + 4\rho_0^2 + \rho_0^2\left(k^2 + 4\rho_0^2\right)^{1/2}\right]}, \tag{48}$$

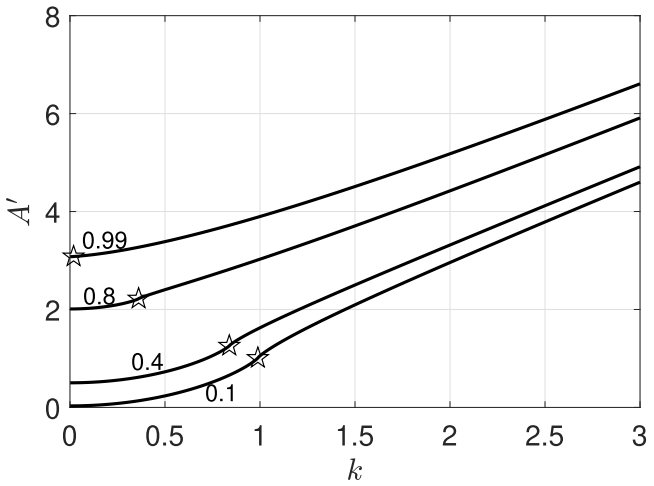

FIG. 8. Plume cross-sectional area as a function of k for different source radii, i.e., $\rho_0 = 0.1$, 0.4, 0.8, and 0.99. The stars indicate where $k = 1 - \rho_0^2$.

which reduces to Eq. (21) in the limit $\rho_0 \to 0$. In the near- and far-field limits, Eq. (48) reduces to

$$f_e \to \begin{cases} \frac{\pi\rho_0(\rho_0+2)}{\rho_0+1}, & k \to 0, \\ \pi k^{1/2}, & k \to \infty, \end{cases} \tag{49}$$

respectively. In the latter case, we reproduce the limit associated with $\rho_0 = 0$. In the former case, Rf_e tends to the plume source perimeter ($2\pi R\rho_0$) times $\frac{\rho_0+2}{2(\rho_0+1)}$. The term $\frac{\rho_0+2}{2(\rho_0+1)}$ decreases monotonically as ρ_0 increases, which, as expected, indicates less entrainment associated with a large plume source.

We retain the governing equations described in Secs. II C 1 and II C 3, however, with entrainment fluxes given by Eqs. (47) and (48). The procedure for solving the original model with Eq. (20), the revised model with Eq. (23) and the curvature method with Eq. (31), by replacing Eq. (21) with Eq. (48), is similar to that described in Sec. II C 3. A slight difference is that the initial guess for k is now vanishingly small, e.g., 10^{-12}, and the range of integration is $0 \leqslant \hat{z} \leqslant 5$.

D. Representative results

Representative solutions showing the vertical velocities [panels (a) and (b)] and volume fluxes [panels (c) and (d)] with $\rho_0 = 0.1$ and 0.6 and $\Gamma_0 = 1$ are illustrated in Fig. 9. In general, both the revised model and the curvature method predict a smaller vertical velocity but a greater volume flux (and therefore greater breadth) compared to the original model. For $\rho_0 = 0.1$, the vertical velocity predicted by the original model [Fig. 9(a)] overshoots the far-field similarity solution, which is consistent with Fig. 3(a) of R16. This overshoot is however absent in Fig. 9(b) for which $\rho_0 = 0.6$.

Table II lists the characteristic heights, i.e., $\hat{z}_{fc}$, $\hat{z}_{fm}$, and $\hat{z}_{vf}$, for the flows considered in Fig. 9. The method of determining the far-field virtual origin is identical to that in R16, with a positive value denoting a distance below the actual source. Due to the enhanced entrainment considered in the revised model and the curvature method, both Eqs. (24) and (31) predict somewhat lower elevations for full merger than does the original model.

The evolution of $\Gamma_m = 2^{1/2}\Gamma(z)$ for the original, revised and curvature models is illustrated in Fig. 10. Figure 10(a) shows that for plumes with $\rho_0 = 0.1$ and $\Gamma_0 = 1$, Γ_m oscillates about unity using the original model and the revised model with $S = 1$. For the original model, a similar oscillation is observed in Fig. 10(b) where, consistent with Fig. 9, ρ_0 is increased from 0.1 to

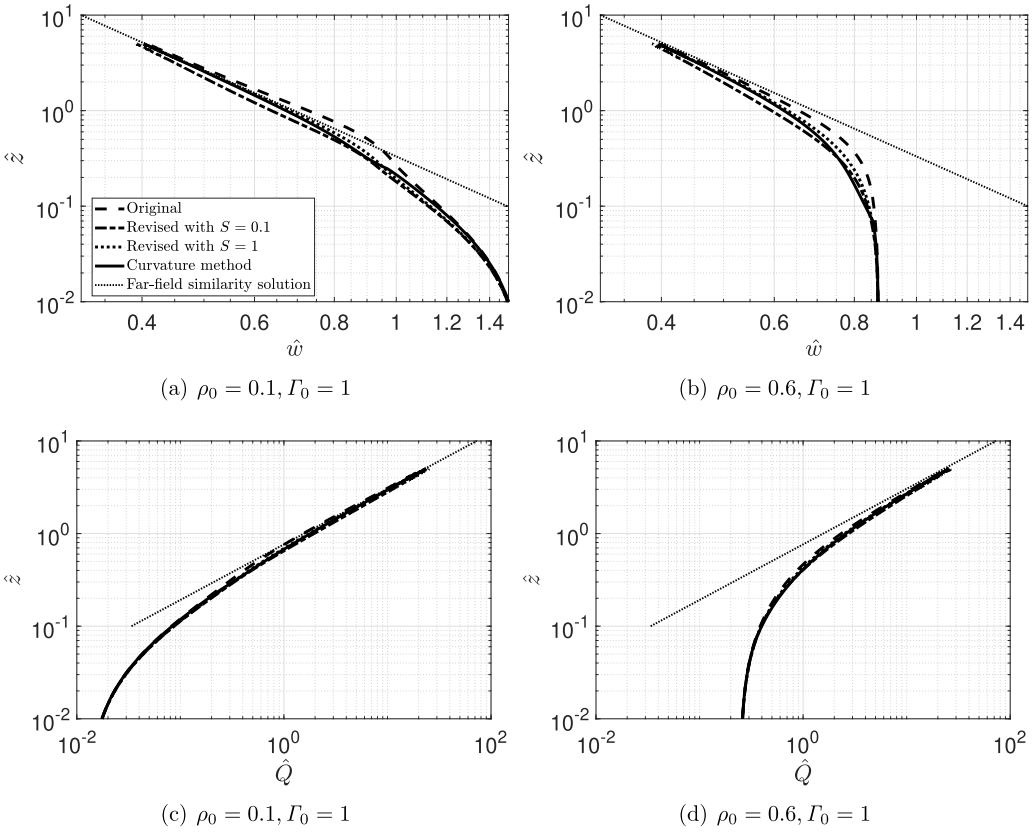

(a) $\rho_0 = 0.1, \Gamma_0 = 1$ (b) $\rho_0 = 0.6, \Gamma_0 = 1$

(c) $\rho_0 = 0.1, \Gamma_0 = 1$ (d) $\rho_0 = 0.6, \Gamma_0 = 1$

FIG. 9. Nondimensional vertical velocity [panels (a) and (b)] and volume flux [panels (c) and (d)] as functions of height for the original model (dashed curve), the revised model with $S = 0.1$ (solid curve) and with $S = 1$ (dotted curve) and the curvature method (solid curve). The thin dotted lines denote the far-field similarity solutions for $\hat{w}$ and $\hat{Q}$, respectively.

0.6. According to R16, the pronounced dip to $\Gamma_m < 1$ using the original model [Figs. 10(a) and 10(b)] indicates that entrainment is relatively low around $\hat{z}_{fm}$. As a result, the plume is forced to accelerate to the far-field limit, which is reflected by the overshooting of the far-field similarity solution in Fig. 9(a). By contrast, the curvature method and the revised model with $S = 0.1$ tend more smoothly to the far-field similarity solution in that they avoid overshoot for ρ_0 large and small.

TABLE II. Heights of first contact and full merger and the far-field virtual origin correction for the source conditions considered in Fig. 9. Values correspond, in sequence, to the original model Eq. (19), the revised model Eq. (24) with $S = 0.1$ and with $S = 1$, and the curvature method Eq. (31).

Source parameters	$\hat{z}_{fc}$	$\hat{z}_{fm}$	$\hat{z}_{vf}$
$\rho_0 = 0.1, \Gamma_0 = 1$	0.27, 0.23, 0.24, 0.25	0.56, 0.46, 0.49, 0.48	−0.05, 0.19, 0.06, 0.09
$\rho_0 = 0.6, \Gamma_0 = 1$	0.08, 0.07, 0.07, 0.07	0.34, 0.28, 0.30, 0.28	0.24, 0.45, 0.33, 0.36

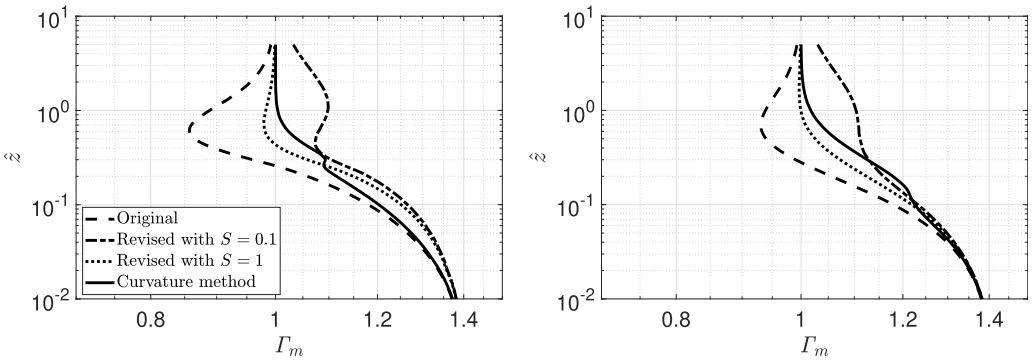

(a) $\rho_0 = 0.1$, $\Gamma_0 = 1$ (b) $\rho_0 = 0.6$, $\Gamma_0 = 1$

FIG. 10. Evolution of Γ_m for $\rho_0 = 0.1$ and $\rho_0 = 0.6$ with $\Gamma_0 = 1$.

E. Effects of varying ρ_0 and Γ_0

Further to the analysis in Sec. IV D, we now consider a range of ρ_0 and Γ_0. Moreover, we focus exclusively on the curvature method in this (and the next) section. The evolution of Γ_m for different Γ_0 with $\rho_0 = 0.1$ and $\rho_0 = 0.6$ is illustrated in Figs. 11(a) and 11(b), respectively. For a small plume source, e.g., $\rho_0 = 0.1$, Fig. 11(a) shows that all Γ_m, even for a highly forced plume ($\Gamma_0 = 0.2$), first exceed then relax to unity. By contrast, and for a much larger source e.g., $\rho_0 = 0.6$, Fig. 11(b) shows that plumes arising from a moderately ($\Gamma_0 = 0.4$) or highly ($\Gamma_0 = 0.2$) forced source remain forced until pure plume balance is achieved in the far field. This is due to more rapid plume merger for larger plume sources whereby the combined plume at the point of first contact exhibits $\Gamma_m < 1$.

Another parameter of interest is the effective entrainment, which is defined as the ratio of the volume flux of two merging (nonideal) plumes to the total volume flux of the same two plumes, now isolated [8]. For a single isolated axisymmetric plume, the entrainment rate is expressed as

$$E = 2\pi b \alpha w, \tag{50}$$

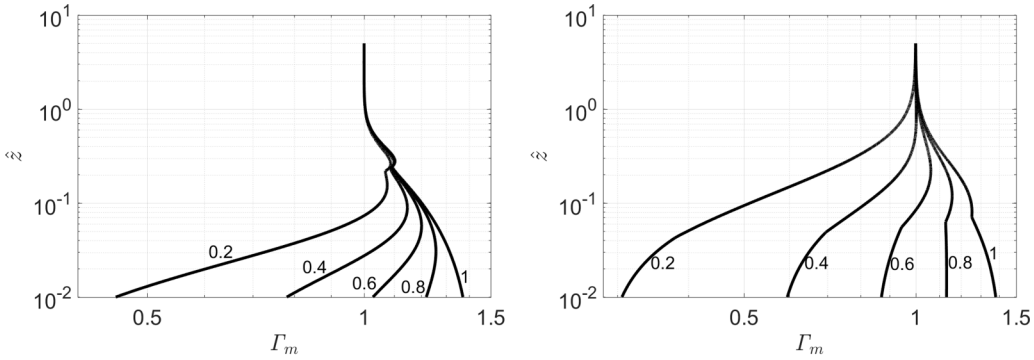

(a) $\rho_0 = 0.1$ (b) $\rho_0 = 0.6$

FIG. 11. Evolution of Γ_m for $\rho_0 = 0.1$ and $\rho_0 = 0.6$ with $\Gamma_0 = 0.2$, 0.4, 0.6, 0.8, and 1.

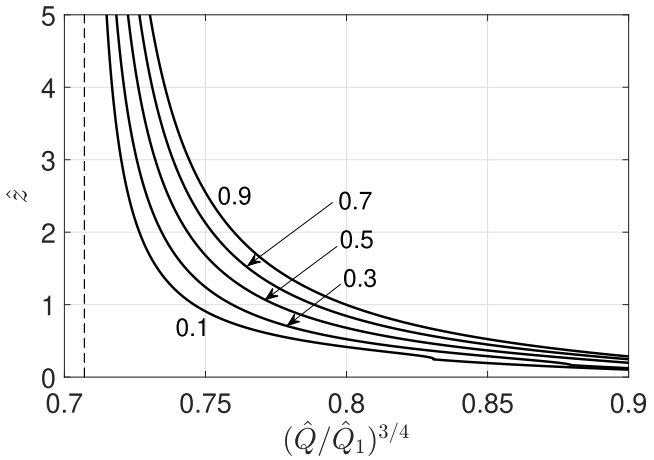

FIG. 12. Effective entrainment with $\Gamma_0 = 1$ and $\rho_0 = 0.1$, 0.3, 0.5, 0.7, and 0.9. The thin dashed vertical line denotes the far-field limit, $2^{-1/2}$.

where b is the mean plume radius. Following the nondimensionalization in Sec. II C 3, the governing equations for an isolated plume are given as

$$\frac{d\hat{w}_1}{d\hat{z}} = \frac{1}{\hat{w}_1\hat{Q}_1} - \frac{2\pi^{1/2}\hat{w}_1^{3/2}}{\hat{Q}_1^{1/2}}, \tag{51}$$

$$\frac{d\hat{Q}_1}{d\hat{z}} = 2\pi^{1/2}\hat{w}_1^{1/2}\hat{Q}_1^{1/2}, \tag{52}$$

where the subscript 1 denotes a single isolated plume. Figure 12 shows the evolution of the effective entrainment, expressed as $(\hat{Q}/\hat{Q}_1)^{3/4}$, for $\Gamma_0 = 1$ and different ρ_0. It is evident from Fig. 12 that the larger the plume source, the greater the effective entrainment. This result seems counter-intuitive: two plumes are deemed to be less affected by each other if they are set apart by a greater distance (i.e., ρ_0 is small). This paradoxical behavior arises because small plumes tend to be more heavily distorted in terms of their cross-sectional area and this, in turn, depresses ambient entrainment. By contrast, a comparison between Figs. 7(a) and 7(b) reveals that larger plume sources suffer from less distortion, i.e., departure from the original circular shape. As a consequence, they admit more (effective) ambient entrainment than their small ρ_0 counterparts.

F. Comparison with the saline plume experiment of Davis *et al.* [26]

Davis *et al.* [26] studied the dilution characteristics of single and multiple plumes using water tank experiments. In their experiments, the densimetric Froude number is defined as $\mathrm{Fr}_0 = w_0/(g_0' D)^{1/2}$ where D is the plume source diameter, thus we can relate Fr_0 to Γ_0 as follows:

$$\Gamma_0 = \frac{5}{16\alpha}\mathrm{Fr}_0^{-2}. \tag{53}$$

With $\alpha = 0.12$, $\mathrm{Fr}_0 = 6$ corresponds to $\Gamma_0 = 0.072$, which represents a highly forced plume at the source. A single spacing ratio corresponding to $\rho_0 = 0.75$ is considered by Davis *et al.* [26]. The comparison between their experimental measurements and the curvature method is shown in Fig. 13 where we plot the variation of the plume volume flux with elevation. Although only limited experimental data are available, the agreement between theory and experiment is robust.

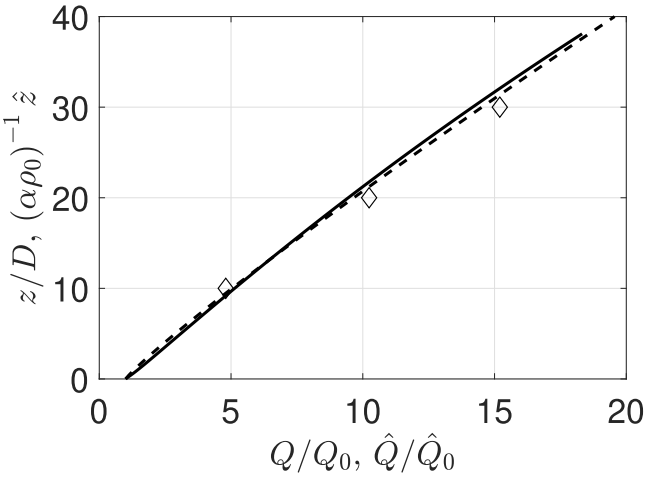

FIG. 13. Comparison of the curvature method with the experimental data of Davis *et al.* [26]. The solid curve denotes the curvature method with $\alpha = 0.14$. The open diamonds correspond to volume flux measurements made at $z/D_0 = 10$, 20, and 30. The dashed curve is a curve fit to all the experimental data of Davis *et al.* [26].

G. Extreme case of $\rho_0 = 1$

The extreme case with $\rho_0 = 1$ is of interest because the plumes start to contact at the source, whilst the plume sources are circular. A similar situation is, of course, the merger of two plumes whose cross-sections remain circular, which is assumed in the models of Kaye and Linden [7] and Cenedese and Linden [8]. Therefore, and for $\rho_0 = 1$, we argue that the merging plume is likely to be approximated by the region above the "touching height" (a.k.a. the height of first contact) in the piecewise model of Cenedese and Linden [8]. Note that the characteristic length scale is the centerline distance between the two plume centers at the touching height not at the level of the near-field virtual source. Following (2.5) and (2.10) in Cenedese and Linden [8], we first give the piecewise model and its prediction for half of the total volume flux of the two plumes, i.e.,

$$\hat{Q} = \begin{cases} \left(\frac{9}{10}\right)^{1/3} \frac{3}{5}\pi^{2/3}(1.643\hat{z} + 0.465), & \hat{z} \leqslant 0.107, \\ \left(\frac{9}{5}\right)^{1/3} \frac{3}{5}\pi^{2/3}(\hat{z} + 0.560)^{5/3}, & \hat{z} > 0.107, \end{cases} \tag{54}$$

where $\hat{z} = 0$ now represents the touching height at which point the two plumes are expected to be fully self-similar, i.e., $\Gamma(\hat{z} = 0) = 1$ and $\hat{z} = 0.107$ represents the height of full merger. The evolution of the volume flux obtained from the models of Secs. II–IV and Cenedese and Linden's piecewise counterpart Eq. (54) is shown in Fig. 14. In all cases, excellent overlap is noted.

V. APPLICATIONS TO COOLING TOWERS

A. Governing equations

For cooling tower plumes, buoyancy derives from temperature and humidity. As such, and in addition to the volume and momentum fluxes defined, respectively, as $Q = A\,w$ and $M = A\,w^2$, we must also define an excess temperature flux, $\Theta = A\,w(t_p - t_a)$ where t denotes the air dry-bulb temperature, an excess specific humidity flux, $H = A\,w(q_p - q_a)$ where q denotes the specific humidity, and an excess specific liquid moisture flux, $W = A\,w\,(\sigma_p - \sigma_a)$ where σ denotes the specific liquid moisture. Subscripts p and a denote the plume and the ambient, respectively. The

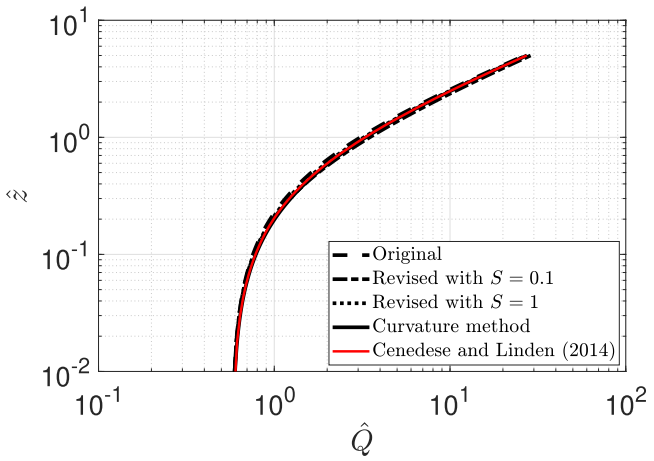

FIG. 14. Plume volume flux for the limiting case of $\rho_0 = 1$ and $\Gamma_0 = 1$.

buoyancy flux is defined as

$$F = A\,w\,g' = A\,w\,g\left(1 - \frac{t_{v,a}}{t_{v,p}}\right), \tag{55}$$

where the plume virtual temperature and ambient virtual temperature, $t_{v,p}$ and $t_{v,a}$, are, respectively, defined as follows [27]:

$$t_{v,p} = \left(t_a + 273.15 + \frac{\Theta}{Q}\right)\left[1 + 0.608\left(q_a + \frac{H}{Q}\right) - \frac{W}{Q}\right], \tag{56}$$

$$t_{v,a} = (t_a + 273.15)\,(1 + 0.608\,q_a - \sigma_a). \tag{57}$$

Here we consider t_a values measured in degrees Celsius and $\sigma_a = 0$ signifying an ambient devoid of liquid moisture. Note that even in a stationary and unstratified ambient, the buoyancy flux of a moist plume is not always constant due to the possibility of condensation. We consider the dimensional form of the governing equations, which read as follows:

$$\frac{dQ}{dz} = E, \tag{58}$$

$$\frac{dM}{dz} = A\,g', \tag{59}$$

$$\frac{d}{dz}\left(\Theta - \frac{L_v}{c_{pa}}\,W\right) = 0, \tag{60}$$

$$\frac{d}{dz}(H + W) = 0, \tag{61}$$

where the latent heat of condensation, measured in J/g, is $L_v = L_v(t) = 4.1868\,[597.31 - 0.57\,t]$ with t measured in degrees Celsius, and $c_{pa} = 1.006$ J/(g K) representing the specific heat of air at constant pressure [3]. The set of Eqs. (58)–(61) is consistent with the governing equation for moist plumes specified by Eq. (19) of Morton [28]. Some authors, e.g., Woods [29], have used the full form of the energy conservation equation including enthalpy, kinetic energy and potential energy [cf. Woods's Eq. (4)]. When the mixing process is adiabatic, the full form equation reduces to the conservation equation for thermal energy, i.e., Eq. (60).

TABLE III. Representative operating and environmental conditions for cooling towers [30].

Variable symbol	Variable name	Value (unit)
P_a	Ambient pressure at the top of the cooling tower	101 325 (Pa)
t_a	Ambient temperature	6 (°C)
RH_a	Ambient relative humidity	65 (%)
t_w	Wet cooling temperature	30 (°C)
t_d	Dry cooling temperature	20 (°C)
w_0	Stack exit velocity	6 and 10 (m/s)
A_0	Stack exit area	71.3 (m^2)
d	Distance between cell centers	14.3 (m)
$\frac{\dot{m}_d}{\dot{m}_w}$	Ratio of the dry to wet air mass flow rate	0.3 and 0.6
n	Number of cooling tower cells	2

B. Representative results

Table III lists the input parameters to be used in assessing the heights of full merger for the present model and also for the WK78 model. According to Eq. (22), and assuming $\alpha = \alpha_p = 0.117$ [31], the source flux-balance parameters are, respectively, $\Gamma_0 = 0.52$ and $\Gamma_0 = 0.57$ for $\frac{\dot{m}_d}{\dot{m}_w} = 0.6$ and $\frac{\dot{m}_d}{\dot{m}_w} = 0.3$ where, in both cases, we have assumed a stack exit velocity of $w_0 = 6$ m/s. The counterpart values for Γ_0 with $w_0 = 10$ m/s are 0.19 and 0.20, respectively. Here $\frac{\dot{m}_d}{\dot{m}_w}$ specifies the ratio between dry (sensible) cooling to wet (evaporative) cooling in a hybrid wet/dry cooling tower—see Li and Flynn [32] for additional details. In WK78, the composite plume post-merger is a combination of a central slot plume and two half round plumes at the two ends—see Fig. 2(c). The entrainment coefficient for the central slot plume is $\alpha_l = 0.147$ and the counterpart coefficient for the two half round plumes is, consistent with the above discussion, $\alpha_p = 0.117$. Therefore, the effective entrainment coefficient for the plume post merger is, on average, between α_p and α_l.

To examine the difference between the WK78 model, Rooney's original and revised models and the curvature method, we plot the height of full merger, $\hat{z}_{fm} = \alpha_p z_{fm}/d$, using the four

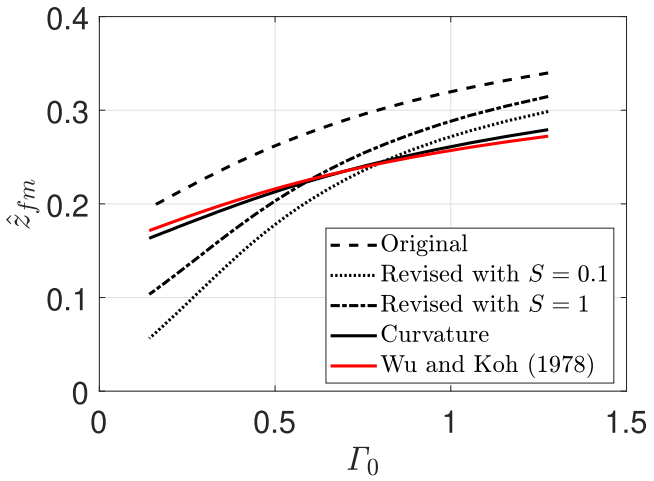

FIG. 15. Height of full merger, $\hat{z}_{fm}$, as a function of the source flux-balance parameter, Γ_0, with $\frac{\dot{m}_d}{\dot{m}_w} = 0.3$. Note that the variation in Γ_0 corresponds to the variation in the cooling tower exit velocity, w_0. Meanwhile, all other parameters correspond to the values given in Table III.

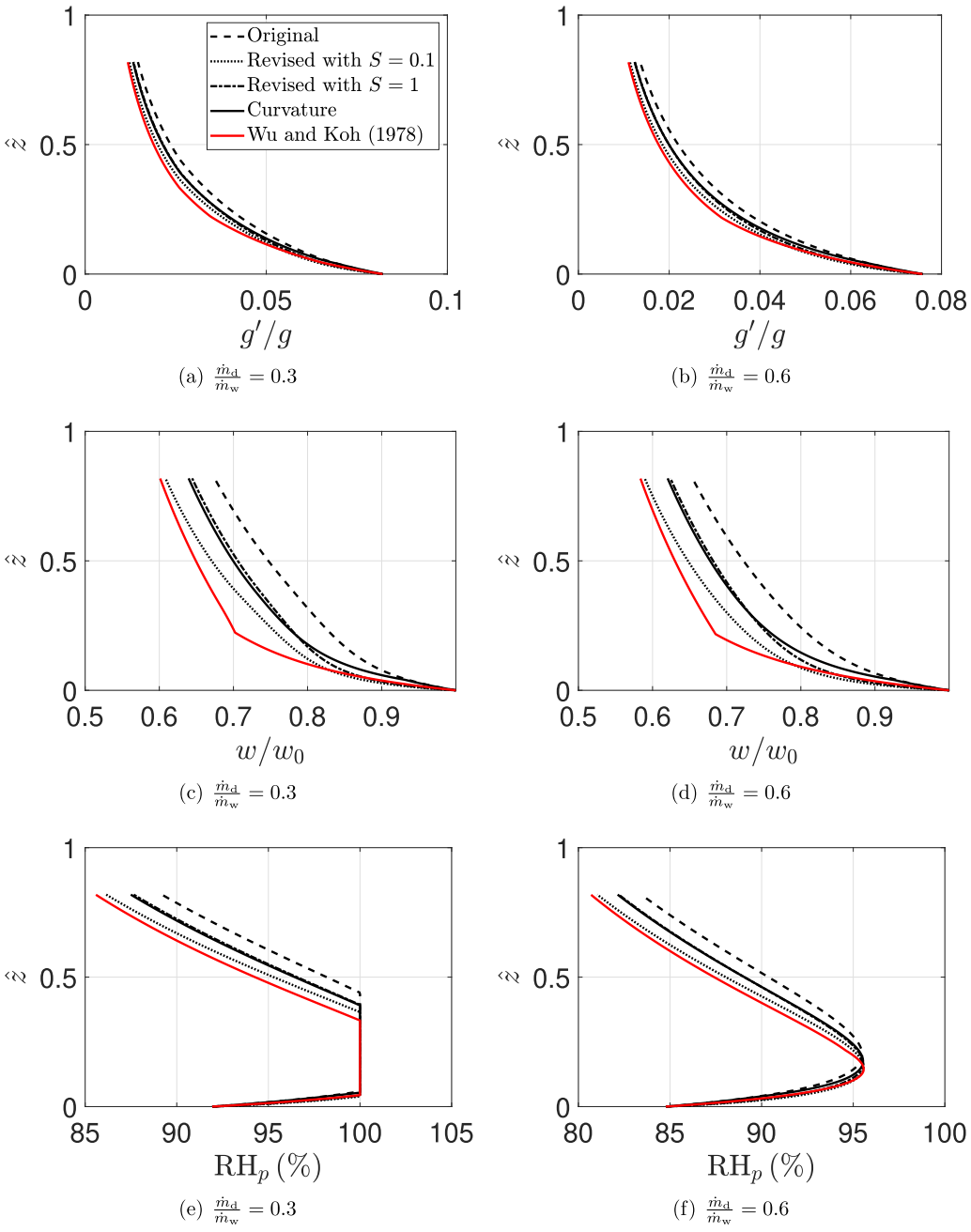

(a) $\frac{\dot{m}_\mathrm{d}}{\dot{m}_\mathrm{w}} = 0.3$ (b) $\frac{\dot{m}_\mathrm{d}}{\dot{m}_\mathrm{w}} = 0.6$

(c) $\frac{\dot{m}_\mathrm{d}}{\dot{m}_\mathrm{w}} = 0.3$ (d) $\frac{\dot{m}_\mathrm{d}}{\dot{m}_\mathrm{w}} = 0.6$

(e) $\frac{\dot{m}_\mathrm{d}}{\dot{m}_\mathrm{w}} = 0.3$ (f) $\frac{\dot{m}_\mathrm{d}}{\dot{m}_\mathrm{w}} = 0.6$

FIG. 16. Nondimensional plume reduced gravity [panels (a) and (b)], vertical velocity [panels (c) and (d)] and relative humidity [panels (e) and (f)] as functions of height above the stack exit. The stack exit velocity is $w_0 = 6\,\mathrm{m/s}$.

aforementioned approaches as functions of the source flux-balance parameter, Γ_0, for $\frac{\dot{m}_d}{\dot{m}_\mathrm{w}} = 0.3$—see Fig. 15. The range for Γ_0 is 0.13 to 1.22 (w_0 is 4 to 12 m/s) to ensure that the source flow spans the range between forced and slightly lazy. Similar profiles are predicted in case of $\frac{\dot{m}_d}{\dot{m}_\mathrm{w}} = 0.6$ (not

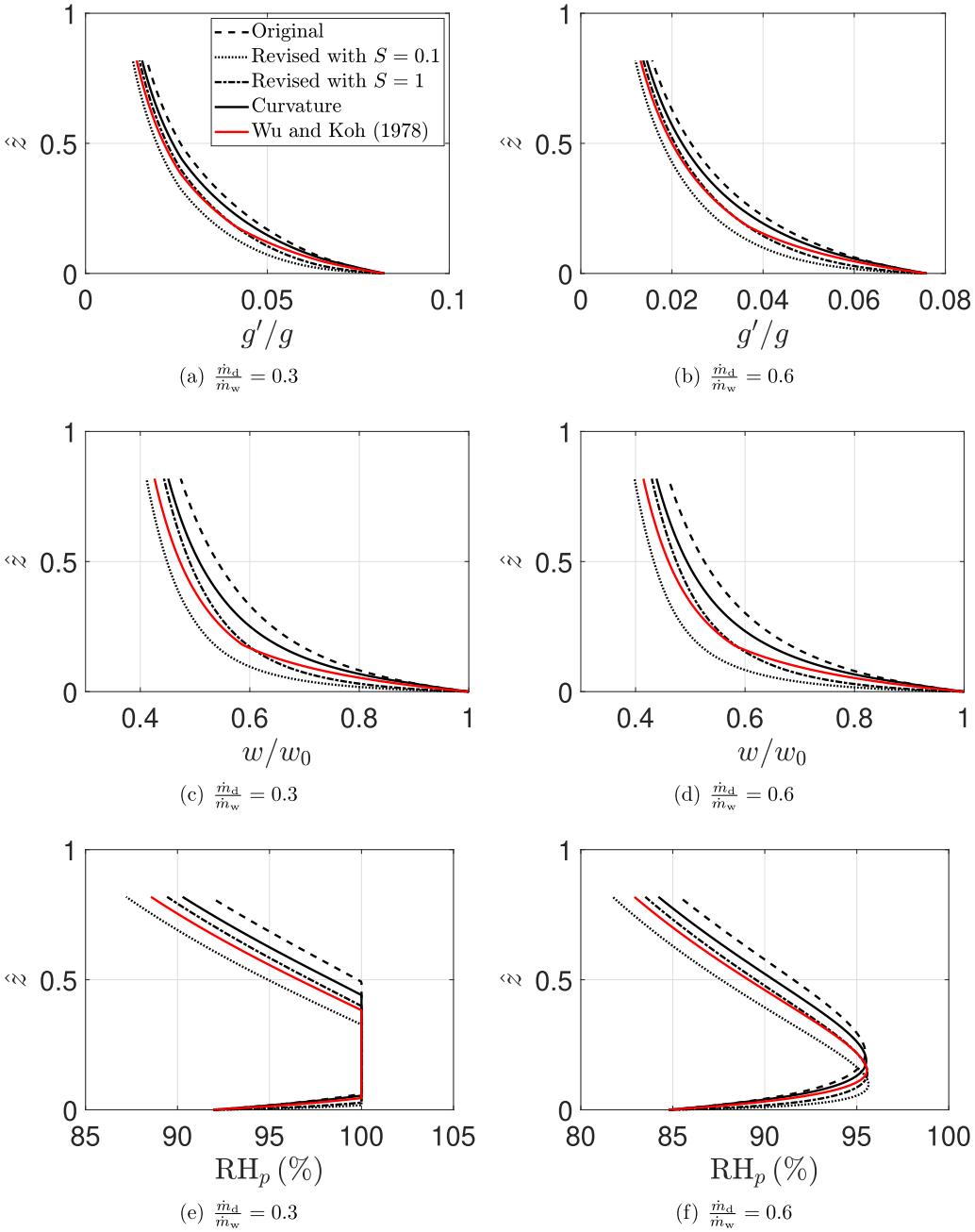

(a) $\frac{\dot{m}_\mathrm{d}}{\dot{m}_\mathrm{w}} = 0.3$ (b) $\frac{\dot{m}_\mathrm{d}}{\dot{m}_\mathrm{w}} = 0.6$

(c) $\frac{\dot{m}_\mathrm{d}}{\dot{m}_\mathrm{w}} = 0.3$ (d) $\frac{\dot{m}_\mathrm{d}}{\dot{m}_\mathrm{w}} = 0.6$

(e) $\frac{\dot{m}_\mathrm{d}}{\dot{m}_\mathrm{w}} = 0.3$ (f) $\frac{\dot{m}_\mathrm{d}}{\dot{m}_\mathrm{w}} = 0.6$

FIG. 17. As in Fig. 16 but with a stack exit velocity of $w_0 = 10\,\mathrm{m/s}$.

shown), which indicates that the moisture effect on plume dynamics is modest. For $\Gamma_0 \lesssim 0.7$, the WK78 model predicts slightly greater $\hat{z}_{fm}$ than does the curvature method although the difference is small. The original model always predicts the greatest $\hat{z}_{fm}$ among the five models. However, and for $\Gamma_0 \approx 1$, the revised models predict somewhat greater $\hat{z}_{fm}$ than does the WK78 model. This reduced entrainment in the revised model is consistent with Eqs. (23) and (24) which require entrainment

to decrease as Γ_m increases. For smaller Γ_0, the revised models, with their increased entrainment, predict smaller $\hat{z}_{fm}$ than does the WK78 model.

The strong agreement between the curvature method and the WK78 model evident in Fig. 15 is all the more encouraging given the prevalence of the latter in atmospheric dispersion models [17,33]. Unfortunately, and whereas the red and (solid) black curves show strong overlap when considering $\hat{z}_{fm}$, greater differences arise when examining other metrics. For example, Fig. 16 shows the plume reduced gravity, vertical velocity and relative humidity (RH) of the WK78 versus original and revised models and the curvature method where we consider $w_0 = 6\,\mathrm{m/s}$. Similar results but with $w_0 = 10\,\mathrm{m/s}$, are presented in Fig. 17. Figures 16(a)–16(d) indicate that the WK78 (original) model predicts the greatest (smallest) dilution rate. Accordingly, Fig. 16(e) shows that the WK78 (original) model predicts the shortest (longest) visible plume. For a larger exit velocity, i.e., $w_0 = 10\,\mathrm{m/s}$, however, Fig. 17 shows that the revised model with $S = 0.1$ produces the greatest dilution rate, even compared to the WK78 model. By contrast, the curvature method always predicts a greater visible plume length thus less dilution rate compared to WK78. It should be emphasized that the WK78 model overestimates the entrainment rate in the near field because it does not properly account for plume interaction and the corresponding reduced entrainment that follows therefrom. Consequently, and in contrast to Rooney's revised model, we see that there exists a consistent offset between the curvature method and WK78, this because the curvature method predicts a lower rate of dilution than does WK78. In spite of this, the overall comparison, accounting for the data of Figs. 15 to 17, is satisfactorily robust.

VI. CONCLUSIONS

The present manuscript extends the theory in Rooney [12,14] to describe the merging of two area source plumes in an unstratified ambient. The plume boundary is defined by the contours defined by Eq. (34); these contours grow from the circumference of a circular source of arbitrary size. The height of full merger is here defined as the height at which the combined plume boundary is no longer concave. Another contribution of this work is to compare this height of full merger with the alternative definition (and model predictions) due to Wu and Koh [3]. In adapting the turbulent plume equations of Morton *et al.* [19], Wu and Koh [3] argued that the point of merger should be regarded as that elevation where the area of the central rectangle equals the sum of areas of the two half round plumes—see Fig. 2(c).

Rooney's revised model incorporates a correction factor Eq. (24) that depends on the velocity potential contour (k), flux-balance parameter (Γ_m), and a free parameter (S). To generalize and simplify the correction factor, an alternate entrainment assumption, i.e., the so-called curvature method, is herein proposed. It allows one to specify the rate of entrainment exclusively from the geometry of the plume boundary. In turn, predictions of the height of full merger derived from the curvature method and from Rooney's revised model are broadly consistent with the experimental results of Kaye and Linden [7]. Similarly positive agreement is also noted upon comparing the curvature method and the experimental data collected by Davis *et al.* [26].

For small, forced and pure plume sources, plume merger allows the plume to transition to a lazy plume regime then approach the far-field pure plume limit. By contrast, and for larger and highly forced plume sources, the merging plume directly approaches the far-field limit, dynamics that are similar to an isolated plume. For fixed Γ_0, small plume sources yield less effective entrainment as compared to larger sources, this as a result of the entrainment-inhibiting distortion of the plume cross-sectional area that is experienced for small z.

The application of the curvature method to adjacent cooling tower plumes yields good agreement with predictions of the merger height made by Wu and Koh [3]. Meanwhile, representative results (Figs. 16 and 17) show that the curvature method consistently predicts a slightly greater visible plume length than does the model of Wu and Koh [3], the latter exhibiting generally good agreement with independently collected laboratory and field data [34,35].

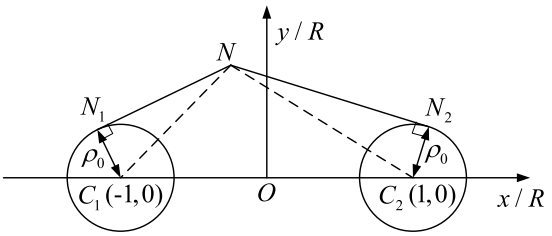

FIG. 18. Schematic illustrating the geometric details associated with Eq. (34). The left and right circles are centered at C_1 $(-1, 0)$ and C_2 $(1, 0)$, respectively, and both have radius ρ_0. From the point N, the straight lines NN_1 and NN_2 are tangent to the circles centered at C_1 and C_2, respectively; N_1 and N_2 are the respective tangent points.

The present model is restricted to two plumes with the same source height, source size and source strength. Even with this restriction, the model cannot describe the contraction above a lazy plume with $\Gamma_0 > 5/2$. Nonetheless, as a first approximation, lazy plumes may be assumed to interact only above the necking zone. Topics of future research interest are to apply the present model to merging plumes in case of ambient stratification and to merging turbulent fountains. For adjacent forced plumes in a linearly stratified ambient, He and Lou [15] directly applied Rooney's theory whereas the finite source effect and the fountain-like behavior at the plume top were not considered. For moderately spaced turbulent fountains, the downflowing outer plumes are expected to merge thus influencing the fountain rise height.

ACKNOWLEDGMENTS

Financial support was generously provided by Natural Sciences and Engineering Research of Canada (NSERC), International Cooling Tower Inc., and the China Scholarship Council (CSC). A helpful discussion with G. G. Rooney is also acknowledged, with thanks.

APPENDIX A: A NOTE ON THE DERIVATION OF EQ. (34)

Underpinning Eq. (34) are some geometrical details, which we highlight in Fig. 18. The lengths of the straight lines, $|NC_1|$, $|NC_2|$, $|NN_1|$, and $|NN_2|$, are given as follows:

$$|NC_1| = |Z' + 1|, \quad |NC_2| = |Z' - 1|, \tag{A1}$$

$$|NN_1| = \left(|Z' + 1|^2 - \rho_0^2\right)^{1/2}, \quad |NN_2| = \left(|Z' - 1|^2 - \rho_0^2\right)^{1/2}, \tag{A2}$$

where $Z' = x/R + iy/R$ corresponds to the position N. The product $|NC_1||NC_2| = k$ is consistent with Eq. (2). A set of curves resulting from this latter equality are called Cassini ovals [36]; these curves are shown in the right-half plane in Fig. 4. For $\rho_0 > 0$, and to avoid any curves within the two circles shown in Fig. 18, we consider not $|NC_1||NC_2|$ but rather $|NN_1||NN_2|$. Doing so yields $(|Z' + 1|^2 - \rho_0^2)^{1/2}(|Z' - 1|^2 - \rho_0^2)^{1/2} = k$, which is consistent with Eq. (34). As observed in Figs. 4 and 7, a half lemniscate is realized in the right-half plane when $k = 1$ and $k = 1 - \rho_0^2$ using Eqs. (2) and (34), respectively.

APPENDIX B: NOTE ON $n \geqslant 3$ AREA SOURCE PLUMES

According to R16, the velocity potential contours for n ideal source plumes spaced equally around a circle of radius R are specified by

$$\rho^{2n} - 2\rho^n \cos n\theta + 1 = k^2. \tag{B1}$$

The left-hand side of Eq. (B1) can be decomposed as follows:

$$\rho^{2n} - 2\rho^n \cos n\theta + 1 = \prod_{m=1}^{n} \left[\rho^2 - 2\rho \cos\left(\theta + \frac{2(m-1)\pi}{n} \right) + 1 \right]. \tag{B2}$$

To introduce a source of finite radius, we must now include a factor of ρ_0. Doing so after first combining Eqs. (B1) and (B2) yields

$$\prod_{m=1}^{n} \left\{ \rho^2 - 2\rho \cos\left[\theta + \frac{2(m-1)\pi}{n} \right] + 1 - \rho_0^2 \right\} = k^2. \tag{B3}$$

On substituting $\rho = 0$ in Eq. (B3), we find that $k = (1 - \rho_0^2)^{n/2}$, which corresponds to the point of first contact. This implies that first contact between adjacent plumes is accelerated if ρ_0 and/or n increases. Unfortunately, it is not straightforward to obtain analytical solutions to Eq. (B3) with $n \geqslant 3$.

APPENDIX C: ENTRAINMENT FLUX FOR SOURCES WITH $\rho_0 > 0$

From Eqs. (34) and (12), we can determine the flow speed as

$$q = \frac{m}{2\pi R} \frac{2\rho}{\left(k^2 + 2\,\rho_0^2\,\rho^2 - \rho_0^4 + 2\rho_0^2 \right)^{1/2}}. \tag{C1}$$

Analogous to R16, the volume of fluid entrained across any velocity potential contour C is

$$E = \int_C q\, dl = \frac{mI}{2\pi}, \tag{C2}$$

where

$$I = \int_C \frac{2\rho}{\left(k^2 + 2\rho_0^2\rho^2 - \rho_0^4 + 2\rho_0^2 \right)^{1/2}}\, dl' \tag{C3}$$

and

$$dl' = \frac{2\left\{ \rho^4 + \left(-\rho^4 + \rho_0^2\rho^2 \right)\left[\left(1 - \rho_0^2 \right)^2 - k^2 - \rho_0^2\rho^2 \right] \right\}^{1/2}}{\left\{ 4\rho^4 - \left[\rho^4 - 2\rho_0^2\rho^2 + \left(1 - \rho_0^2 \right)^2 - k^2 \right] \right\}^{1/2}} d\rho \tag{C4}$$

$$= \frac{\left[k^2 + 2\rho_0^2(1 + \cos 2\theta) \right]^{1/2} \left\{ \rho_0^2 + \cos 2\theta \pm \left[k^2 - \sin^2 2\theta + 2\rho_0^2(1 + \cos 2\theta) \right]^{1/2} \right\}^{1/2}}{\left[k^2 - \sin^2 2\theta + 2\rho_0^2(1 + \cos 2\theta) \right]^{1/2}} d\theta. \tag{C5}$$

Using Eqs. (35) or (36), the right-hand side of Eq. (C3) can be expressed as a function of ρ or θ, respectively. Note that Eq. (C2) does not account for the nonorthogonality between the streamlines and the plume boundary defined by Eq. (34). For $\rho_0 > 0$, the velocity component that is normal to the contours defined by Eq. (34) satisfies

$$\frac{dy}{dx} = \frac{\left(1 + \rho_0^2 - \rho^2 \right) \cos\theta}{\left(1 - \rho_0^2 + \rho^2 \right) \sin\theta} = -\frac{u_\perp}{v_\perp}. \tag{C6}$$

Note that Eq. (C6) reduces to Eq. (11) in the limit of vanishingly small ρ_0. By incorporating the angle, θ', between the velocity vectors ($\mathbf{u}$ and $\mathbf{u}_\perp$) expressed, respectively, by Eqs. (11) and (C6), Eq. (C2) can be rewritten as

$$E = \int_C q_\perp dl = \int_C q \cos\theta' dl = \frac{mI}{2\pi}, \tag{C7}$$

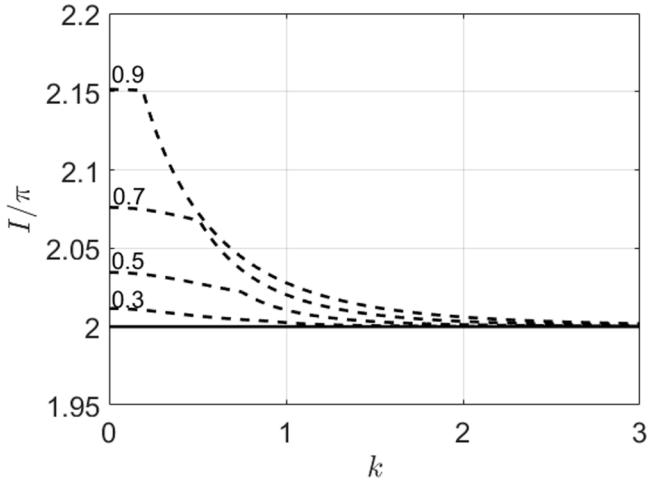

FIG. 19. Flux integral as a function of k for various ρ_0. Dashed curves follow Eq. (C2), whereas the solid line follows Eq. (C7).

where $q_\perp$ is the flow speed normal to the plume boundary and

$$\cos\theta' = \frac{\mathbf{u}}{\|\mathbf{u}\|}\cdot\frac{\mathbf{u}_\perp}{\|\mathbf{u}_\perp\|} = \frac{k^2+\rho_0^2\rho^2-\rho_0^4+2\rho_0^2+\rho_0^2\cos 2\theta}{\left(k^2+2\,\rho_0^2\,\rho^2-\rho_0^4+2\rho_0^2\right)^{1/2}\left[k^2+2\rho_0^2(1+\cos 2\theta)\right]^{1/2}}. \tag{C8}$$

Of course, (C8) reduces to $\cos\theta' = 1$ when $\rho_0 = 0$.

Solutions for I determined, respectively, by Eqs. (C2) and (C7) are presented as functions of k in Fig. 19. Note that, once the speed normal to the plume boundary ($q_\perp$) is adopted, $I = 2\pi$ and therefore $E = m$. When the total speed (q) is applied instead, we find from the dashed curves of Fig. 19 a deviation from $I = 2\pi$ for small k. Not surprisingly, the deviation grows with ρ_0.

[1] O. Abessi and P. J. Roberts, Multiport diffusers for dense discharges, J. Hydraul. Eng. **140**, 04014032 (2014).
[2] P. F. Linden, The fluid mechanics of natural ventilation, Ann. Rev. Fluid Mech. **31**, 201 (1999).
[3] F. H. Wu and R. C. Koh, *Mathematical Model for Multiple Cooling Tower Plumes* (US Environmental Research Laboratory, Office of Research and Development, 1978).
[4] P. F. Linden and N. B. Kaye, Interacting turbulent plumes in a naturally ventilated enclosure, Int. J. Ventilat. **4**, 301 (2006).
[5] P. Lindahl and K. Mortensen, Plume abatement—The next generation, CTI J. **31**, 8 (2010).
[6] G. I. Taylor, Flow induced by jets, J. Aero. Sci. **25**, 464 (1958).
[7] N. B. Kaye and P. F. Linden, Coalescing axisymmetric turbulent plumes, J. Fluid Mech. **502**, 41 (2004).
[8] C. Cenedese and P. F. Linden, Entrainment in two coalescing axisymmetric turbulent plumes, J. Fluid Mech. **752** (2014).
[9] A. C. Lai and J. H. Lee, Dynamic interaction of multiple buoyant jets, J. Fluid Mech. **708**, 539 (2012).
[10] T.-H. Shih, W. W. Liou, A. Shabbir, Z. Yang, and J. Zhu, A new k-ϵ eddy viscosity model for high Reynolds number turbulent flows-Model development and validation, Comput. Fluids **24**, 227 (1995).
[11] P. C. Yannopoulos, Advanced integral model for groups of interacting round turbulent buoyant jets, Environ. Fluid Mech. **10**, 415 (2010).
[12] G. Rooney, Merging of a row of plumes or jets with an application to plume rise in a channel, J. Fluid Mech. **771**, R1 (2015).

[13] J. W. M. Bush and A. W. Woods, Experiments on buoyant plumes in a rotating channel, Geophys. Astrophys. Fluid Dyn. **89**, 1 (1998).
[14] G. Rooney, Merging of two or more plumes arranged around a circle, J. Fluid Mech. **796**, 712 (2016).
[15] Z. He and Y. Lou, Integral model for multiple forced plumes arranged around a circle in a linearly stratified environment, Phys. Rev. Fluids **4**, 123501 (2019).
[16] L. R. Davis, *Analysis of Multiple Cell Mechanical Draft Cooling Towers* (US Environmental Protection Agency, Washington, D.C., 1975).
[17] A. Policastro, W. Dunn, and R. Carhart, A model for seasonal and annual cooling tower impacts, Atmos. Environ. **28**, 379 (1994).
[18] S. Li, A. Moradi, B. Vickers, and M. Flynn, Cooling tower plume abatement using a coaxial plume structure, Int. J. Heat Mass Transfer **120**, 178 (2018).
[19] B. R. Morton, G. I. Taylor, and J. S. Turner, Turbulent gravitational convection from maintained and instantaneous sources, Proc. R. Soc. London Ser. A **234**, 1 (1956).
[20] N. B. Kaye, Turbulent plumes in stratified environments: A review of recent work, Atmos. Ocean **46**, 433 (2008).
[21] T. Van den Bremer and G. Hunt, Universal solutions for Boussinesq and non-Boussinesq plumes, J. Fluid Mech. **644**, 165 (2010).
[22] B. R. Morton, Forced plumes, J. Fluid Mech. **5**, 151 (1959).
[23] G. Hunt and T. Van den Bremer, Classical plume theory: 1937–2010 and beyond, IMA J. Appl. Math. **76**, 424 (2011).
[24] G. Hunt and N. Kaye, Virtual origin correction for lazy turbulent plumes, J. Fluid Mech. **435**, 377 (2001).
[25] W. D. Baines, A technique for the direct measurement of volume flux of a plume, J. Fluid Mech. **132**, 247 (1983).
[26] L. Davis, M. A. Shirazi, and D. L. Slegel, *Experimental Simulation of Single and Multiple Cell Cooling Tower Plumes*, Vol. 1 (Environmental Protection Agency, Office of Research and Development, 1977).
[27] K. A. Emanuel, *Atmospheric Convection* (Oxford University Press on Demand, Oxford, UK, 1994).
[28] B. Morton, Buoyant plumes in a moist atmosphere, J. Fluid Mech. **2**, 127 (1957).
[29] A. W. Woods, A model of the plumes above basaltic fissure eruptions, Geophys. Res. Lett. **20**, 1115 (1993).
[30] D. G. Kröger, *Air-cooled Heat Exchangers and Cooling Towers* (PennWell Books, Tulsa, OK, 2004).
[31] E. List, Turbulent jets and plumes, Ann. Rev. Fluid Mech. **14**, 189 (1982).
[32] S. Li and M. R. Flynn, Coaxial plumes in a windy ambient with applications to cooling towers, J. Wind Eng. Industr. Aerodynam. **196**, 104054 (2020).
[33] L. R. Davis, *Fundamentals of Environmental Discharge Modeling* (CRC Press, Boca Raton, FL, 1998).
[34] L.-N. Fan, Turbulent buoyant jets into stratified or flowing ambient fluids, Ph.D. thesis, California Institute of Technology, 1967.
[35] S. Carpenter, J. Leavitt, F. W. Thomas, J. A. Frizzola, and M. E. Smith, Full-scale study of plume rise at large coal-fired electric generating stations, J. Air Pollut. Contr. Assoc. **18**, 458 (1968).
[36] M. Karataş, A multifoci closed curve: Cassini oval, its properties, and applications, Doğuş Üniv. Dergisi **14**, 231 (2013).